Volume 12 | Number 16 | 21 August 2025

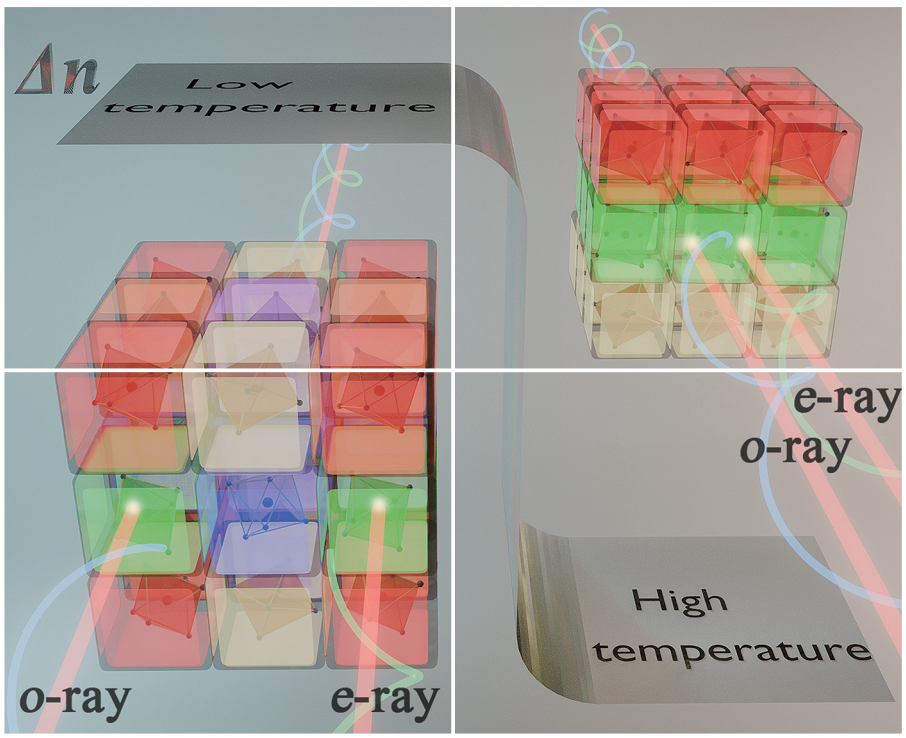

INORGANIC CHEMISTRY

FRONTIERS

CCS 中国化学会 CHINESE CHEMICAL SOCIETY
PEKING UNIVERSITY 1898
ROYAL SOCIETY OF CHEMISTRY
rsc.li/frontiers-inorganic

INORGANIC CHEMISTRY FRONTIERS

RESEARCH ARTICLE

View Article Online
View Journal | View Issue

Cite this: *Inorg. Chem. Front.*, 2025, **12**, 4776

Large birefringence switching in a new zero-dimensional cyanide perovskite ferroelastic material†

Jun-Si Zhou,‡ Luan-Ying Ji,‡ Shu-Yi Liu and Xiao-Gang Chen *

Received 26th April 2025,
Accepted 23rd June 2025

DOI: 10.1039/d5qi01019e

rsc.li/frontiers-inorganic

Cyanide perovskites have demonstrated significant potential in the design of molecular ferroelastic, ferroelectric, and multiferroic materials. However, previous research has primarily focused on three-dimensional (3D) cyanide perovskites, which are structurally constrained and exhibit limited diversity. In this study, we synthesized a new zero-dimensional (0D) cyanide perovskite ferroelastic material, $(MA)_3[Fe(CN)_6]$ (MA = CH_3NH_3, methylamine), and conducted comprehensive characterization through differential scanning calorimetry (DSC), dielectric measurements, variable-temperature structural analysis, and polarized light microscopy. $(MA)_3[Fe(CN)_6]$ undergoes an isomorphic phase transition with a spontaneous strain of 0.1063. The birefringence at 300 K and 330 K is 0.302@546 nm and 0.022@546 nm, respectively. The substantial birefringence change up to 0.28 mainly originates from the rotational motion of inorganic and organic components. This work establishes a new pathway for designing 0D cyanide perovskite materials.

Introduction

Birefringence is a fundamental optical phenomenon in anisotropic materials, and is characterized by the splitting of incident light into two orthogonally polarized beams with different propagation velocities during transmission.[1] This optical property, which is intrinsically linked to the crystalline structure and symmetry of materials, enables crucial optical polarization state conversions, making birefringent crystals indispensable in optoelectronic applications.[2–5] In recent years, the switching of birefringence by physical means has attracted widespread attention.[6–8] Ferroelastic materials exhibit remarkable potential for diverse applications in sensor technology,[9] actuator systems,[10,11] and shape memory devices,[12] owing to their distinctive characteristics of reversible strain response and stress–strain hysteresis under mechanical stress. The fundamental mechanism of ferroelasticity originates from reversible structural phase transitions and symmetry breaking in the crystal lattice.[13] For optical anisotropic materials, ferroelastic phase transition can change the birefringence properties of materials. $SrTiO_3$ undergoes an $m\bar{3}mF4/mmm$ ferroelastic phase transition, and the linear development of the birefringence near the phase transition is consistent with normal Landau mean-field behaviour. This transition originates from the symmetry breaking during the ferroelastic phase transition.[14] Therefore, birefringence switching can be achieved by adjusting the ferroelasticity of the material.

Organic–inorganic hybrid perovskite materials have attracted wide attention due to their unique structure, environmental friendliness, easy processing, and biocompatibility,[15–21] and have shown great potential in the construction of ferroelastic phase transition materials and birefringence switching materials.[22–29] Recently, Wang *et al.* observed thermal switching birefringence in a two-dimensional (2D) layered hybrid halide perovskite $(C_2N_3H_4)_2PbCl_4$, whose birefringence can be reversibly switched by thermotropic phase transition.[30] Ma *et al.* reported a 2D perovskite ferroelectric, (*N*-methylcyclohexylammonium)$_2PbCl_4$, which has an unusual triple-state switching of birefringence, which involves the variation of the ferroelastic strain and domain in the vicinity of the phase transition.[31] Cyanide perovskites have characteristic cyano groups as bridging ligands, which are coordinated with different metal ions through their carbon atoms and nitrogen atoms. This coordination asymmetry, arising from the differing electronic properties of the nitrogen and carbon atoms, enables the formation of diverse double perovskite structures with the general formula $A_2[B'B''(CN)_6]$, where A represents monovalent cations, B′ represents mono-

Ordered Matter Science Research Center, Nanchang University, 330031, P. R. China. E-mail: chenxg@ncu.edu.cn

† Electronic supplementary information (ESI) available: Fig. S1–S6, Tables S1–S5. CCDC 2442254 and 2442255. For ESI and crystallographic data in CIF or other electronic format see DOI: https://doi.org/10.1039/d5qi01019e

‡ These authors have contributed equally to this work.

valent metals, and B″ represents trivalent metals. This unique electronic structure and coordination chemistry make it exhibit excellent properties in ferroelasticity,[32–38] ferroelectricity,[39,40] dielectric switching,[41–45] and nonlinear optics.[46,47] However, previously reported cyanide perovskite materials have been exclusively limited to three-dimensional (3D) structures.[48–57] The formation of 3D perovskites is determined by Goldschmidt's tolerance factor (t), which greatly limits the structural diversity of 3D perovskites.[58] To overcome these limitations, we propose for the first time to remove alkali metals to design 0D materials, breaking the shackles and providing unlimited possibilities for the development of new 0D cyanide perovskite materials.

In this work, we successfully synthesized a 0D hybrid perovskite ferroelastic material $(MA)_3[Fe(CN)_6]$ (MA = CH_3NH_3, methylamine). To our knowledge, $(MA)_3[Fe(CN)_6]$ represents the first reported cyanide perovskite compound that deviates from the conventional 3D perovskite framework. Notably, this material undergoes isomorphic phase transitions with spontaneous strains of 0.1063. Large spontaneous strain brings a large birefringence switch. The birefringence is 0.302@546 nm and 0.022@546 nm at 300 K and 330 K, respectively. This outstanding birefringence performance has exceeded those of the main commercial birefringence crystals, such as $LiNbO_3$ (Δn = 0.074@546 nm),[59] YVO_4 (Δn = 0.204@532 nm),[60] $CaCO_3$ (Δn = 0.172@532 nm),[61] TiO_2 (Δn = 0.256@546 nm),[62] and α-BaB_2O_4 (Δn = 0.122@546 nm).[63] Its birefringence changes up to 0.28, and such a large birefringence switching comes from the rotation motion of the components with an increase of temperature. This mechanism is fundamentally different from that of the traditional birefringence switching materials, in which the change of optical properties usually comes from the phase transition that causes symmetry breaking.[31,64,65] This novel 0D cyanide perovskite ferroelastic material, featuring significant birefringence switching, demonstrates promising potential for advanced optical applications.

Results and discussion

Synthesis

Silver ferricyanide and methylamine hydrochloride were mixed in deionized water at a molar ratio of 1 : 3, filtered, and the filtrate was placed at room temperature for 5 days to obtain red transparent block crystals (Fig. S1a, ESI†). Fig. S1b (ESI†) demonstrates that the red bulk crystals undergo a distinct color change to yellow upon mechanical grinding into powdered form. This chromatic transition originates from modifications in the optical absorption characteristics of the crystalline material, potentially associated with alterations in the light scattering properties induced by the size reduction process. The phase purity of the synthesized $(MA)_3[Fe(CN)_6]$ compound was confirmed through powder X-ray diffraction (PXRD) analysis conducted at room temperature (Fig. S2, ESI†).

Thermal properties

Thermogravimetric analysis (TGA) was performed on the $(MA)_3[Fe(CN)_6]$ compound within the temperature range of 300–1000 K (Fig. S3, ESI†). The results demonstrate that $(MA)_3[Fe(CN)_6]$ exhibits excellent thermal stability, maintaining structural integrity up to 470 K. To explore the potential phase transition behavior of $(MA)_3[Fe(CN)_6]$, the differential scanning calorimetry (DSC) experiment was performed. As shown in Fig. 1a, one distinct pair of thermal anomalies was observed during the heating and cooling cycles, demonstrating the reversible nature of the phase transition. Notably, the pronounced thermal hysteresis observed during the heating and cooling cycles represents a characteristic feature of first-order phase transitions. For the convenience of description, the crystal structure with a temperature below 319 K is called the low-temperature phase (LTP), and above 319 K is called the high-temperature phase (HTP).

Dielectric properties

The phase transition of $(MA)_3[Fe(CN)_6]$ was further verified by measuring the change of the real part (ε') of the complex value of permittivity with temperature at a frequency of 1 MHz. Fig. 1b shows the temperature dependence of ε' during both

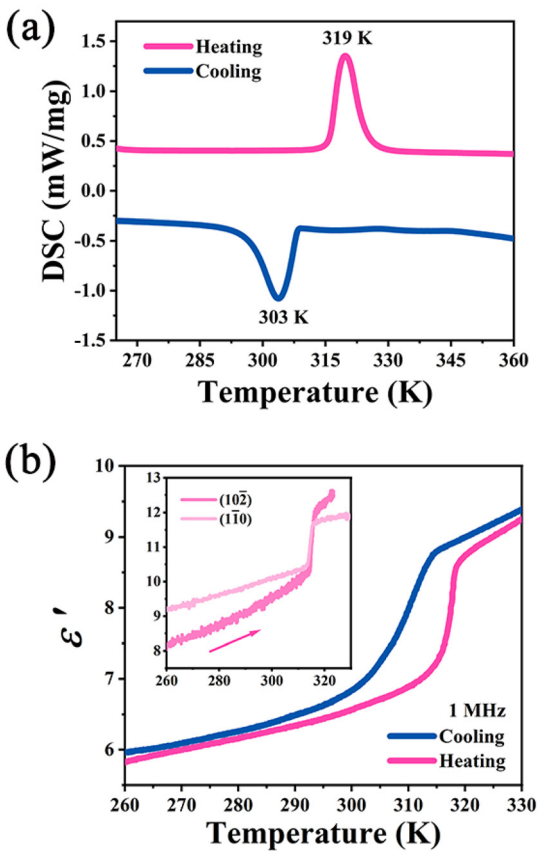

Fig. 1 (a) DSC curve; (b) the change of ε' with temperature at a frequency of 1 MHz. Inset: the variation of ε' values with temperature along the crystallographic (10$\bar{2}$) and (1$\bar{1}$0) planes at a frequency of 1 MHz.

heating and cooling cycles at an applied frequency of 1 MHz. Within the narrow temperature range of 310–325 K, a distinct ladder-like anomaly is observed. During the heating process, the ε' value increases rapidly from 7.1 at 313 K to 8.8 at 320 K, confirming the occurrence of a phase transition. The inset shows the variation of ε' values with temperature along the crystallographic $(10\bar{2})$ and $(1\bar{1}0)$ planes (Fig. S4, ESI†) at 1 MHz. Compared with the powder pellet test, single-crystal measurements along both crystallographic directions exhibit higher ε' values and more pronounced dielectric anomalies at the phase transition, which shows the anisotropy of the crystal.

Structural analyses

To investigate the structural origin of phase transition behavior, variable-temperature single-crystal X-ray diffraction analysis was performed on $(MA)_3[Fe(CN)_6]$ and the crystal structures were obtained at 300 K and 360 K. The crystallographic data are summarized in Table S1 (ESI)†.

In the LTP (Fig. 2a), $(MA)_3[Fe(CN)_6]$ crystallizes in the $P\bar{1}$ space group of the triclinic system, belonging to the $\bar{1}$ (C_i) point group with the following unit cell parameters: a = 14.0643 Å, b = 16.3738 Å, c = 16.5138 Å, α = 60.714°, β = 76.502°, γ = 75.116°. The Fe^{3+} coordinates with six CN^- to form the $[Fe(CN)_6]^{3-}$ octahedron complex with different orientations, the distance between the Fe^{3+} and the characteristic CN^- is d(Fe–C) = 1.927–1.955 Å, the angle between C–Fe–C is 87.6°–93.8° (Tables S2 and S3, ESI†), and the MA^+ cations are located around the $[Fe(CN)_6]^{3-}$ octahedron complexes, effectively isolating the $[Fe(CN)_6]^{3-}$ octahedron so that the $[Fe(CN)_6]^{3-}$ octahedron exists independently. The nitrogen atoms on the MA^+ cations and the cyanide ligands in the $[Fe(CN)_6]^{3-}$ octahedron function as hydrogen bond donors and acceptors, respectively, forming intermolecular N–H···N hydrogen bonds (d (N–N) = 2.798–2.921 Å) (Table S4, ESI†). The rich hydrogen bond network connects the MA^+ cations with the $[Fe(CN)_6]^{3-}$ octahedron, thereby maintaining molecular stability.

In the HTP (Fig. 2b), $(MA)_3[Fe(CN)_6]$ still crystallizes in the triclinic system $P\bar{1}$ space group and the cell parameters are a = 8.3596 Å, b = 14.2847 Å, c = 14.3096 Å, α = 81.042°, β = 74.897°, γ = 88.154°. The distance between the Fe^{3+} and the characteristic CN^- is d(Fe–C) = 1.911–1.950 Å, and the angle between C–Fe–C is 88.2°–92.0° (Tables S2 and S3, ESI†); compared with LTP, the $[Fe(CN)_6]^{3-}$ octahedral distortion is reduced. As shown in Fig. 2c, the significant reorientation of $[Fe(CN)_6]^{3-}$ octahedron was observed, showing a temperature-dependent rotation motion. The MA^+ organic cations exhibit two distinct thermal response modes: (1) a cooperative rotational motion synchronizing with the inorganic framework; and (2) some MA^+ cations transform to a two-fold disordered configuration through an order-disorder dynamic transformation.

From the LTP to HTP, the directional degrees of freedom of organic and inorganic components are significantly reduced due to different degrees of rotational motion with increasing

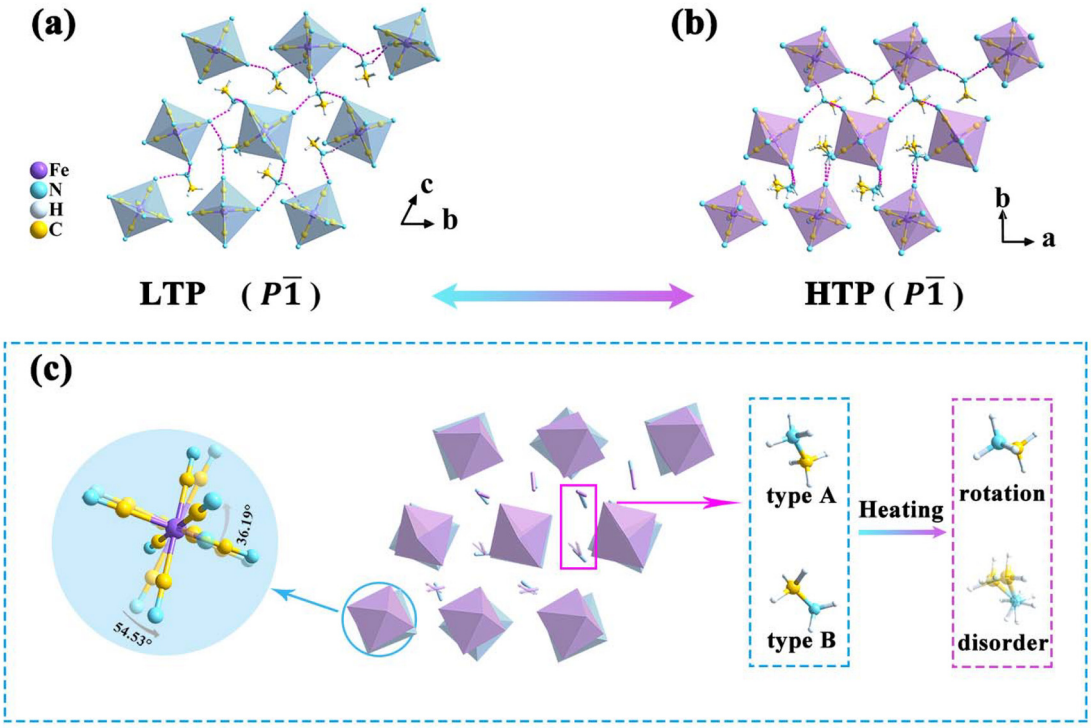

Fig. 2 (a and b) The crystal structure of $(MA)_3[Fe(CN)_6]$ at 300 K, and 360 K. The pink dotted line represents the intermolecular hydrogen bond. (c) The phase transition mechanism of $(MA)_3[Fe(CN)_6]$. The LTP and HTP are distinguished by blue and purple pyramids, respectively. The blue circle indicates the rotation of the $[Fe(CN)_6]^{3-}$ octahedron in the LTP (transparent) and HTP. The blue dotted frame and the purple dotted frame indicate the two types of transitions of MA^+ cations in the LTP and HTP.

temperature. The $[Fe(CN)_6]^{3-}$ octahedron has six different arrangement directions reduced to three, while the MA^+ cation is reduced from twelve to six so that the arrangement of the organic component and the inorganic component becomes neat. Therefore, the phase transition of $(MA)_3[Fe(CN)_6]$ mainly comes from the rotational motion of the molecule, The distortion of the $[Fe(CN)_6]^{3-}$ octahedron and the order–disorder dynamic transition of some cations also contributes to the phase transition. According to the Boltzmann equation $\Delta S = R\ln(N)$, where R represents the gas constant and N denotes the ratio of possible orientations during the phase transition, the calculated value of N at 319 K was 7.976, further indicating that cooperative cation–anion rotational dynamics, rather than solely MA^+ cations disordering, constitutes the principal value of entropy change.

IR and Raman spectroscopy

The infrared (IR) spectrum of $(MA)_3[Fe(CN)_6]$ (Fig. S5, ESI†) was recorded at room temperature. The characteristic vibrational modes of this compound can be compared to those of similar materials containing $[Fe(CN)_6]^{3-}$.[56,66] Hydrogen bonding influences the frequency, strength and the width of vibrations.[67,68] The bands in the high-frequency region, between 3500 and 2600 cm^{-1}, correspond to the stretching vibrations of the N–H groups in the crystal, and the strong and wide characteristics confirm the existence of intermolecular hydrogen bonds. The strong absorption band at 2115 cm^{-1} is assigned to the ν(C≡N) stretching vibration of the CN^- ligand. The strong absorption bands at 1602 cm^{-1} and 1485 cm^{-1} are assigned to the δ(N–H) and δ(C–H) deformation vibration, respectively.

Temperature-dependent Raman spectroscopy results (Fig. S6a and b, ESI†) reveal a reversible phase transition near 320 K, consistent with DSC analysis results. At 270 K, the ν(C≡N) stretching vibration splits into two peaks (2106–2146 cm^{-1}). Upon heating to 320–350 K, these split peaks merge into a single dominant band, with the original splitting being fully restored upon cooling. This completely reversible spectral evolution during thermal cycling indicates temperature-activated rotational motion of the $[Fe(CN)_6]^{3-}$ octahedron corresponds to the six different orientations of the $[Fe(CN)_6]^{3-}$ octahedron in LTP reduced to three in HTP.

Ferroelastic domains

The evolution of ferroelastic domains in $(MA)_3[Fe(CN)_6]$ was observed using a variable-temperature polarized light microscope. At 300 K, the crystal is green and bright under orthogonally polarized light (Fig. 3d), but when the crystal rotates clockwise 49°, it completely darkens (Fig. 3e). As the temperature increases to 330 K, the crystal darkens and exhibits stripe-like ferroelastic domains with bright and dark interphases under orthogonally polarized light (Fig. 3f). When the crystal rotates clockwise 59° (Fig. 3g), it completely darkens and on

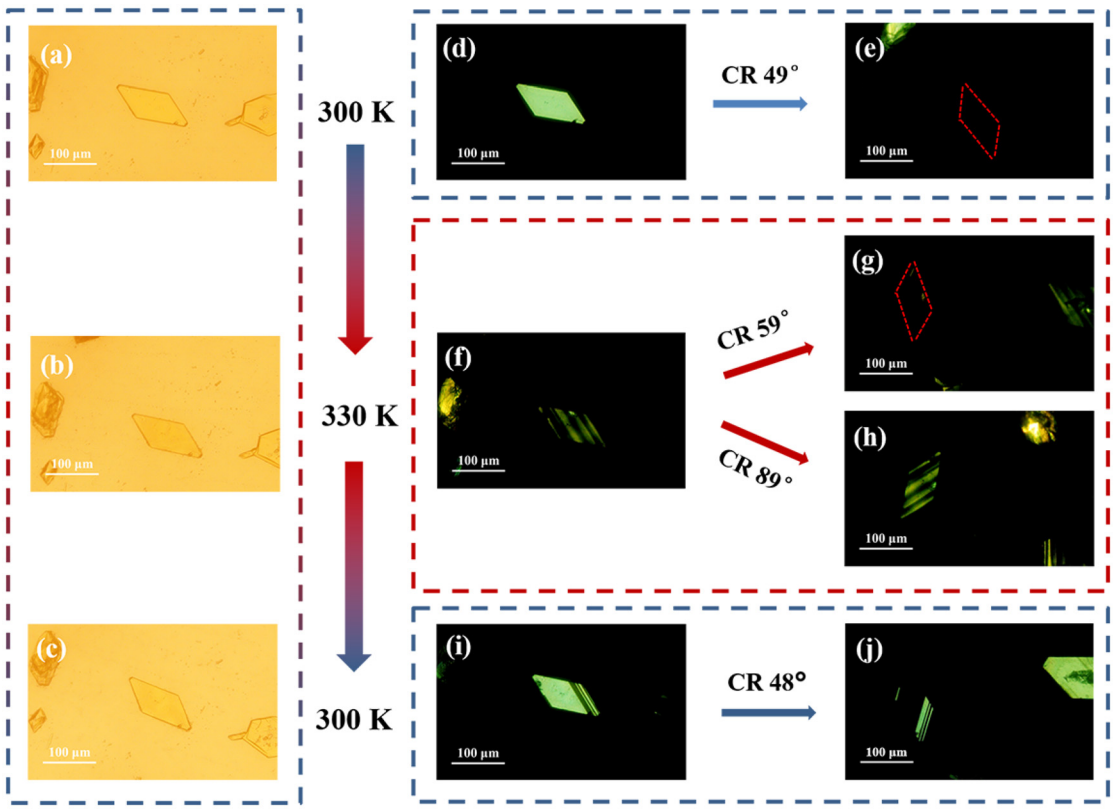

Fig. 3 Ferroelastic domain evolution of $(MA)_3[Fe(CN)_6]$. (a–c) The morphology image of $(MA)_3[Fe(CN)_6]$ under natural light. (d–j) The evolution of ferroelastic domains in $(MA)_3[Fe(CN)_6]$ during heating and cooling cycles. CR represents clockwise rotation.

clockwise rotating 89° (Fig. 3h), the crystal again exhibits stripe-like ferroelastic domains with bright and dark interphases under orthogonally polarized light, which is independent of the surface morphology of the crystal (Fig. 3b). When the crystal is further cooled to 300 K, the crystal becomes bright again under orthogonally polarized light, and the stripe domain pattern changes significantly compared with that at 330 K (Fig. 3i), which is independent of the surface morphology of the crystal (Fig. 3c), and on clockwise rotating 48°, the stripe domain pattern also changes (Fig. 3J). The crystal shows bright (300 K)–dark (330 K)–bright (300 K) changes under orthogonally polarized light during heating and cooling, indicating that the birefringence properties of the crystal have changed.

In addition, according to the variable temperature structure analysis, in LTP and HTP, $(MA)_3[Fe(CN)_6]$ crystallized in same space group ($P\bar{1}$), both located in the ferroelastic phase, but no obvious stripe pattern was observed at 300 K, indicating a single-domain structure for the as-synthesized single crystal. When heated from 300 K (LTP) to 330 K (HTP), the spontaneous strain generated by the phase transition induces the appearance of stripe ferroelastic domains. Notably, upon cooling back to 300 K, the domains persist rather than reverting to the original single-domain orientation. This irreversibility stems from substantial crystal deformation during phase transition, leading to surface defects (Fig. S7, ESI†).[69]

For ferroelastic materials, the spontaneous strain (ε_{ss}) is a crucial parameter for evaluating their ferroelastic properties and it can be calculated based on the crystal lattice parameters. $(MA)_3Fe(CN)_6$ undergoes an isomorphic phase transition, both of which are triclinic before and after the phase transition, the spontaneous strain tensor is given by:[70]

$$[e_{ij}] = \begin{bmatrix} e_{11} & e_{12} & e_{13} \\ 0 & e_{22} & e_{23} \\ 0 & 0 & e_{33} \end{bmatrix} \quad (1)$$

The phase transition brings about a total ε_{ss} of

$$\varepsilon_{ss} = \sqrt{\sum_{ij} e_{ij}^2} \quad (2)$$

For $(MA)_3[Fe(CN)_6]$, according to the cell parameters measured in LTP ($z = 8$) and HTP ($z = 4$), the original a, b, and c axes (8.3596 Å, 14.2547 Å 14.3096 Å) in HTP are transformed into the new a', b', and c' axes (14.3096 Å, 16.7192 Å, 16.7558 Å). α, β, γ (81.942°, 74.897°, 88.154°) are also transformed to α', β', γ' (58.2434°, 75.5672°, 78.8970°). Based on the transformed cell parameters in HTP and the data in LTP, the ε_{ss} is evaluated to be 0.1063 (for more details, see the ESI†). Notably, the ε_{ss} value surpasses that of many reported hybrid perovskite ferroelastics, such as [dimethyl-isopropyl-fluoro ethyl-ammonium][$Cd(SCN)_3$] (0.078),[71] [$(CH_3)_3PCH_2F$][$Cd(SCN)_3$] (0.086),[72] and (nortropinium)[$CdCl_3$] (0.061).[73] Similarly, Xu *et al.* reported a 3D cyanide perovskite ferroelastic $(Me_3NOH)_2(NH_4)[Co(CN)_6]$ with an ε_{ss} of 0.105, primarily originating from the ordered–disordered dynamic transition of organic cations.[74] However, in $(MA)_3[Fe(CN)_6]$, only some organic cations underwent organic–inorganic dynamic transformation yet achieved an approximate ε_{ss} value of 0.1063, which mainly arises from the cooperative rotation of both MA^+ cations and $[Fe(CN)_6]^{3-}$ anions in the lattice.

Birefringence properties

The birefringence was measured under a polarizing microscope with a Berek compensator, using a pre-selected thin crystal plate of $(MA)_3[Fe(CN)_6]$ (Fig. S8a, ESI†). Birefringence occurs after polarized light passes through the measured crystal and two polarized lights are produced with polarization directions perpendicular to each other. Birefringence can be obtained from the following equation:

$$R = |N_e - N_o| \times T = \Delta n \times T \quad (3)$$

where, R, N_e, N_o, Δn, and T represent the optical path difference, extraordinary refractive index, ordinary refractive index, birefringence, and thickness of the sample, respectively. Based on the single-crystal XRD, the single crystal used for measurement can be determined as the (001) crystal plane of $(MA)_3[Fe(CN)_6]$, and the thickness of the $(MA)_3[Fe(CN)_6]$ sample is 6.06 μm (Fig. S8b, ESI†). Fig. 4a and b show the single crystal at 300 K under orthogonal polarized light with a Berek compensator after achieving complete extinction, respectively. Fig. 4d and e separately show the same single crystal at 330 K under orthogonal polarized light with a Berek compensator after achieving complete extinction, and the chiaroscuro inversion of adjacent domains can be observed (one domain appears bright while the other appears dark), which is consistent with the opposite birefringence of the adjacent ferroelastic domain. The optical path difference at 546 nm is 1831.89 nm at 300 K. However, the optical path difference decreases to 133.32 nm at 546 nm at 330 K. According to eqn (3), the birefringence is 0.302@546 nm and 0.022@546 nm at 300 K and 330 K, respectively. This is consistent with the phenomenon observed in the ferroelastic measurement. To our knowledge, this birefringence of $(MA)_3[Fe(CN)_6]$ is relatively large compared with the reported organic–inorganic hybrid birefringence crystals (Table S5, ESI†).

Within the temperature range of 300–360 K, the material demonstrates a significant birefringence switching amplitude, with a birefringence change up to 0.28 (from 0.302@546 nm to 0.022@546 nm). Notably, this phenomenon represents a unique mechanism that fundamentally differs from traditional symmetry-breaking birefringence switch materials.[30,31,64] For instance, Chen *et al.* reported a cyanide perovskite birefringence-switching material, $[C_3H_5FNH_2]_2[(NH_4)Fe(CN)_6]$, where the NH_4^+ cations form hydrogen bonds with the N atoms of cyanide groups to construct a 3D framework. The birefringence change up to 0.08 (from 0.08@546 nm to zero), originates primarily from the symmetry breaking from the anisotropic triclinic phase to the isotropic cubic phase caused by the order-disorder phase transition.[65] However, $(MA)_3[Fe(CN)_6]$ undergoes an isomorphic phase transition while preserving its

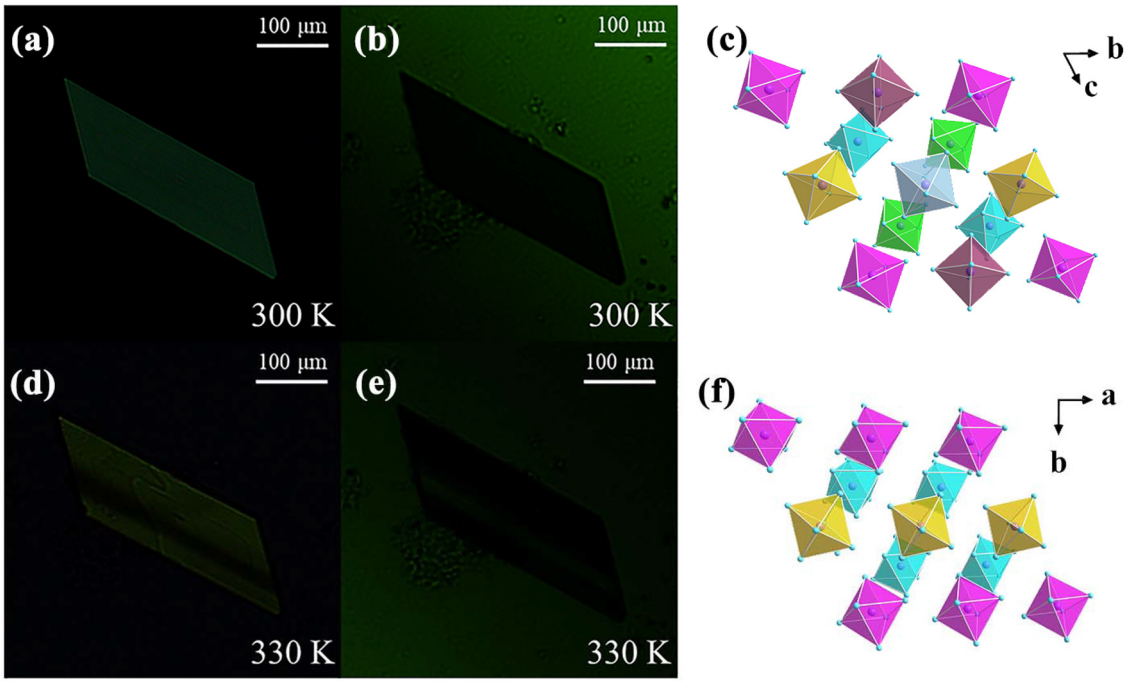

Fig. 4 (a) Single crystal of $(MA)_3[Fe(CN)_6]$ under the orthogonally polarized light at 300 K. (b) Single crystal of $(MA)_3[Fe(CN)_6]$ achieving complete extinction at 300 K. (c) The octahedron stacking diagram in the LTP. (d) Single crystal of $(MA)_3[Fe(CN)_6]$ under the orthogonally polarized light at 330 K. (e) Single crystal of $(MA)_3[Fe(CN)_6]$ achieving complete extinction at 330 K. (f) The octahedron stacking diagram in HTP. In (c) and (f), distinct color schemes are employed to differentiate the various conformational states of the octahedron.

crystal symmetry. As shown in Fig. 4c and f, the stacking diagrams of the $[Fe(CN)_6]^{3-}$ octahedron exhibit distinct differences between the LTP and HTP. In LTP, the octahedron adopts six distinct orientation states. Upon heating, cooperative rotation of the $[Fe(CN)_6]^{3-}$ octahedron occurs, resulting in alignment along three preferred orientations in HTP. This structural evolution results in decreased crystallographic anisotropy, which consequently modifies the birefringence properties of the crystal. Therefore, the birefringence switching is primarily attributed to the rotational motion of organic and inorganic components during thermal excitation. This corresponds to the ε_{ss} of the crystal.

Conclusions

In summary, we have developed a novel 0D cyanide perovskite material, $(MA)_3[Fe(CN)_6]$, which represents a new class of ferroelastic materials exhibiting both above-room-temperature phase transition and significant birefringence switching capabilities. Through comprehensive characterization, including variable-temperature single-crystal structural analysis, polarized light microscopy, thermal analysis, and dielectric measurements, we have established a detailed understanding of its phase transition mechanism. The material demonstrates remarkable birefringence values of 0.302@546 nm at 300 K and 0.022@546 nm at 330 K, exceeding those of the main commercial birefringence crystals. The substantial birefringence change up to 0.28 originates from the rotational motion of inorganic and organic components. This work provides a new idea for the design of new 0D cyanide perovskite materials.

Author contributions

J.-S. Zhou conceived the study and wrote the manuscript. L.-Y. Ji synthesized the samples and carried out thermal and electrical experiments. S.-Y. L performed general characterization. X.-G. Chen carried out X-ray characterization and guided this work.

Conflicts of interest

There are no conflicts to declare.

Data availability

The data supporting this article have been included as part of the ESI.† The X-ray crystallographic structures have been deposited at the Cambridge Crystallographic Data Centre (deposition numbers CCDC: 2442254 and2442255)†.

Acknowledgements

This work was supported by the National Key R&D Program of China (2024YFA1509300), the National Natural Science

Foundation of China (22201120) and Gan Po Juncai Support Program – the Academic and Technical Leader Training Program in Major Disciplines (20243BCE51149).

References

1 A. Tudi, S. Han, Z. Yang and S. Pan, Potential optical functional crystals with large birefringence: Recent advances and future prospects, *Coord. Chem. Rev.*, 2022, **459**, 214380.
2 Z.-Y. Xie, L.-G. Sun, G.-Z. Han and Z.-Z. Gu, Optical Switching of a Birefringent Photonic Crystal, *Adv. Mater.*, 2008, **20**, 3601–3604.
3 X. Chen, W.-g. Lu, J. Tang, Y. Zhang, Y. Wang, G. D. Scholes and H. Zhong, Solution-processed inorganic perovskite crystals as achromatic quarter-wave plates, *Nat. Photonics*, 2021, **15**, 813–816.
4 M. A. Kats, P. Genevet, G. Aoust, N. Yu, R. Blanchard, F. Aieta, Z. Gaburro and F. Capasso, Giant birefringence in optical antenna arrays with widely tailorable optical anisotropy, *Proc. Natl. Acad. Sci. U. S. A.*, 2012, **109**, 12364–12368.
5 S. Niu, G. Joe, H. Zhao, Y. Zhou, T. Orvis, H. Huyan, J. Salman, K. Mahalingam, B. Urwin, J. Wu, Y. Liu, T. E. Tiwald, S. B. Cronin, B. M. Howe, M. Mecklenburg, R. Haiges, D. J. Singh, H. Wang, M. A. Kats and J. Ravichandran, Giant optical anisotropy in a quasi-one-dimensional crystal, *Nat. Photonics*, 2018, **12**, 392–396.
6 L. M. Silva, D. L. Silva, M. V. Boas, Y. Bretonniere, C. Andraud and M. G. Vivas, Probing the high performance of photoinduced birefringence in V-shaped azo/PMMA guest–host films, *RSC Adv.*, 2020, **10**, 40806–40814.
7 K. Morimoto, H. Tsujioka, D. Kitagawa and S. Kobatake, Photoreversible Interference Color Modulation to Multicolor in Photochromic Molecular Crystals, *Bull. Chem. Soc. Jpn.*, 2019, **92**, 1299–1304.
8 W. Setaka and K. Yamaguchi, Order–Disorder Transition of Dipolar Rotor in a Crystalline Molecular Gyrotop and Its Optical Change, *J. Am. Chem. Soc.*, 2013, **135**, 14560–14563.
9 X. Ming, F. Liu, Y. Chen, M. Chen, Y. Zhang, B. Liu, X. Wang, Z. Sun, R. Pan, K. Zheng, Y. Dai, Z. Deng, X. He, W. Cao, S. Wang and L. Wang, Elasto-Optic Effect of Lanthanum-Modified Lead Zirconate–Lead Titanate Transparent Ceramics: Application in Optical-Stress Sensors, *Adv. Opt. Mater.*, 2022, **10**, 2201239.
10 Y. Hu, L. You, B. Xu, T. Li, S. A. Morris, Y. Li, Y. Zhang, X. Wang, P. S. Lee, H. J. Fan and J. Wang, Ferroelastic-switching-driven large shear strain and piezoelectricity in a hybrid ferroelectric, *Nat. Mater.*, 2021, **20**, 612–617.
11 B.-D. Liang, C.-C. Fan, C.-D. Liu, C.-Y. Chai, X.-B. Han and W. Zhang, Near-room-temperature martensitic actuation profited from one-dimensional hybrid perovskite structure, *Nat. Commun.*, 2022, **13**, 6599.
12 Y. Ogawa, D. Ando, Y. Sutou and J. Koike, A lightweight shape-memory magnesium alloy, *Science*, 2016, **353**, 368–370.
13 E. K. H. Salje, Ferroelastic Materials, *Annu. Rev. Mater. Res.*, 2012, **42**, 265–283.
14 M. A. Geday and A. M. Glazer, Birefringence of $SrTiO_3$ at the ferroelastic phase transition, *J. Phys.: Condens. Matter*, 2004, **16**, 3303.
15 P.-F. Li, W.-Q. Liao, Y.-Y. Tang, H.-Y. Ye, Y. Zhang and R.-G. Xiong, Unprecedented Ferroelectric–Antiferroelectric–Paraelectric Phase Transitions Discovered in an Organic–Inorganic Hybrid Perovskite, *J. Am. Chem. Soc.*, 2017, **139**, 8752–8757.
16 B. Chen, R. Yu, G. Xing, Y. Wang, W. Wang, Y. Chen, X. Xu and Q. Zhao, Dielectric Engineering of 2D Organic–Inorganic Hybrid Perovskites, *ACS Energy Lett.*, 2024, **9**, 226–242.
17 X.-G. Chen, Y.-Y. Tang, H.-P. Lv, X.-J. Song, H. Peng, H. Yu, W.-Q. Liao, Y.-M. You and R.-G. Xiong, Remarkable Enhancement of Piezoelectric Performance by Heavy Halogen Substitution in Hybrid Perovskite Ferroelectrics, *J. Am. Chem. Soc.*, 2023, **145**, 1936–1944.
18 X.-G. Chen, X.-J. Song, Z.-X. Zhang, H.-Y. Zhang, Q. Pan, J. Yao, Y.-M. You and R.-G. Xiong, Confinement-Driven Ferroelectricity in a Two-Dimensional Hybrid Lead Iodide Perovskite, *J. Am. Chem. Soc.*, 2020, **142**, 10212–10218.
19 F. Thouin, D. A. Valverde-Chávez, C. Quarti, D. Cortecchia, I. Bargigia, D. Beljonne, A. Petrozza, C. Silva and A. R. Srimath Kandada, Phonon coherences reveal the polaronic character of excitons in two-dimensional lead halide perovskites, *Nat. Mater.*, 2019, **18**, 349–356.
20 T. Vijayakanth, D. J. Liptrot, E. Gazit, R. Boomishankar and C. R. Bowen, Recent Advances in Organic and Organic–Inorganic Hybrid Materials for Piezoelectric Mechanical Energy Harvesting, *Adv. Funct. Mater.*, 2022, **32**, 2109492.
21 D.-Y. Li, J.-H. Song, Z.-Y. Xu, Y.-J. Gao, X. Yin, Y.-H. Hou, L.-J. Feng, C.-Y. Yue, H. Fei and X.-W. Lei, Reversible Triple-Mode Switching in Photoluminescence from 0D Hybrid Antimony Halides, *Chem. Mater.*, 2022, **34**, 6985–6995.
22 C.-Y. Su, Y.-F. Yao, Z.-X. Zhang, Y. Wang, M. Chen, P.-Z. Huang, Y. Zhang, W.-C. Qiao and D.-W. Fu, The construction of a two-dimensional organic–inorganic hybrid double perovskite ferroelastic with a high Tc and narrow band gap, *Chem. Sci.*, 2022, **13**, 4794–4800.
23 W. Huang, X. Zhang, Y. Li, Y. Zhou, X. Chen, X. Li, F. Wu, M. Hong, J. Luo and S. Zhao, A Hybrid Halide Perovskite Birefringent Crystal, *Angew. Chem., Int. Ed.*, 2022, **61**, e202202746.
24 J. Zheng, X. Song, Y. Wu, Y. Lian, Y. Li, Q. Xu, Y. Zhou, Z. Wang, L. Wang, J. Luo and S. Zhao, A Highly Optical Anisotropic Hybrid Perovskite for Efficient Manipulation of Light Polarization, *Adv. Funct. Mater.*, 2024, **34**, 2403843.
25 Q. Xu, W. Huang, H. Wang, Y. Li, Y. Zhou, L. Hou, S. Zhao and J. Luo, Designing a Dimension Reduced Hybrid Perovskite with Robust Large Birefringence by Expanding Cationic π-Delocation, *Small*, 2023, **19**, 2304333.
26 C. Su, M. Lun, Y. Chen, Y. Zhou, Z. Zhang, M. Chen, P. Huang, D. Fu and Y. Zhang, Hybrid Optical-Electrical Perovskite Can Be a Ferroelastic Semiconductor, *CCS Chem.*, 2022, **4**, 2009–2019.

27 J. Li, Y. Zhu, P.-Z. Huang, D.-W. Fu, Q.-Q. Jia and H.-F. Lu, Ferroelasticity in Organic–Inorganic Hybrid Perovskites, *Chem. – Eur. J.*, 2022, **28**, e202201005.
28 Q.-R. Meng, W.-J. Xu, W.-H. Hu, H. Ye, X.-X. Chen, W. Yuan, W.-X. Zhang and X.-M. Chen, An unprecedented hexagonal double perovskite organic–inorganic hybrid ferroelastic material: $(piperidinium)_2[KBiCl_6]$, *Chem. Commun.*, 2021, **57**, 6292–6295.
29 T.-Y. Ju, C.-C. Fan, B.-D. Liang, C.-D. Liu, M.-L. Jin, C.-Y. Chai and W. Zhang, Chirality Triggered Biferroicity in a 3D Rubidium Based Perovskite, *Adv. Funct. Mater.*, 2024, **34**, 2316747.
30 Z. Wang, X. Chen, Y. Song, Z. Du, Y. Zhou, M. Li, W. Huang, Q. Xu, Y. Li, S. Zhao and J. Luo, A Two-Dimensional Hybrid Perovskite With Heat Switching Birefringence, *Angew. Chem., Int. Ed.*, 2023, **62**, e202311086.
31 Y. Ma, B. Wang, W. Li, Y. Liu, W. Guo, H. Xu, L. Tang, Q. Fan, J. Luo and Z. Sun, Unusual Triple-State Switching of Thermally Induced Birefringence in a Two-Dimensional Perovskite Ferroelectric, *J. Am. Chem. Soc.*, 2024, **146**, 27287–27292.
32 S.-Q. Hu, M.-Z. Li, Z.-H. Chen, J.-S. Zhou, L.-Y. Ji, Y. Ai and X.-G. Chen, Switchable coordination bonds in 3D cyano-bridged perovskite ferroelastics: achieving the largest leap of symmetry breaking and enhanced dielectric switching performance, *Inorg. Chem. Front.*, 2024, **11**, 4647–4653.
33 M. Rok, G. Bator, B. Zarychta, B. Dziuk, D. Skalecki, W. Medycki and M. Zamponi, Screening ferroelastic transitions in switchable cyano-bridged perovskites: $[CH_3C(NH_2)_2]_2[KM(CN)_6]$, M = Cr^{3+}, Fe^{3+}, Co^{3+}. Crystal structure characterisation, dielectric properties, ^1H NMR and quasielastic neutron scattering studies, *Cryst. Growth Des.*, 2019, **19**, 4526–4537.
34 M. Moskwa, P. Sobieszczyk, J. W. Mikurenda, P. Zieliński and M. Rok, Improper ferroelastic phase transition in a hydrogen-bonded metallocyanide-based $(azetidinium)_2(H_3O)[Co(CN)_6]$ framework, *Chem. Commun.*, 2023, **59**, 5535–5538.
35 W.-J. Xu, Y. Zeng, W. Yuan, W.-X. Zhang and X.-M. Chen, A large room-temperature entropy change in a new hybrid ferroelastic with an unconventional bond-switching mechanism, *Chem. Commun.*, 2020, **56**, 10054–10057.
36 X.-G. Chen, Z.-X. Zhang, Y.-L. Zeng, S.-Y. Tang and R.-G. Xiong, H/F Substitution induced switchable coordination bonds in a cyano-bridged hybrid double perovskite ferroelastic, *Chem. Commun.*, 2022, **58**, 3059–3062.
37 M.-Z. Li, Z.-H. Chen, S.-Q. Hu, J.-S. Zhou, L.-Y. Ji and X.-G. Chen, Hydrogen-bonding engineering in a 3D cyano-bridged double-perovskite ferroelastic greatly improves the phase-transition temperature, *J. Mater. Chem. C*, 2023, **11**, 15952–15958.
38 M. Rok, M. Moskwa, M. Działowa, A. Bieńko, C. Rajnák, R. Boča and G. Bator, Multifunctional materials based on the double-perovskite organic–inorganic hybrid $(CH_3NH_3)_2[KCr(CN)_6]$ showing switchable dielectric, magnetic, and semiconducting behaviour, *Dalton Trans.*, 2019, **48**, 16650–16660.
39 W.-J. Xu, P.-F. Li, Y.-Y. Tang, W.-X. Zhang, R.-G. Xiong and X.-M. Chen, A Molecular Perovskite with Switchable Coordination Bonds for High-Temperature Multiaxial Ferroelectrics, *J. Am. Chem. Soc.*, 2017, **139**, 6369–6375.
40 W.-J. Xu, K. Romanyuk, Y. Zeng, A. Ushakov, V. Shur, A. Tselev, W.-X. Zhang, X.-M. Chen, A. Kholkin and J. Rocha, Statics and dynamics of ferroelectric domains in molecular multiaxial ferroelectric $(Me_3NOH)_2[KCo(CN)_6]$, *J. Mater. Chem. C*, 2021, **9**, 10741–10748.
41 K. Qian, F. Shao, Z. Yan, J. Pang, X. Chen and C. Yang, A perovskite-type cage compound as a temperature-triggered dielectric switchable material, *CrystEngComm*, 2016, **18**, 7671–7674.
42 X. Zhang, X.-D. Shao, S.-C. Li, Y. Cai, Y.-F. Yao, R.-G. Xiong and W. Zhang, Dynamics of a caged imidazolium cation–toward understanding the order-disorder phase transition and the switchable dielectric constant, *Chem. Commun.*, 2015, **51**, 4568–4571.
43 M. Rok, G. Bator, B. Zarychta, B. Dziuk, J. Repeć, W. Medycki, M. Zamponi, G. Usevičius, M. Šimėnas and J. Banys, Isostructural phase transition, quasielastic neutron scattering and magnetic resonance studies of a bistable dielectric ion-pair crystal $[(CH_3)_2NH_2]_2KCr(CN)_6$, *Dalton Trans.*, 2019, **48**, 4190–4202.
44 M. Trzebiatowska, M. Mączka, A. Gągor and A. J. I. C. Sieradzki, Pyrrolidinium-Based Cyanides: Unusual Architecture and Dielectric Switchability Triggered by Order–Disorder Process, *Inorg. Chem.*, 2020, **59**, 8855–8863.
45 W. Zhang, H.-Y. Ye, R. Graf, H. W. Spiess, Y.-F. Yao, R.-Q. Zhu and R.-G. Xiong, Tunable and Switchable Dielectric Constant in an Amphidynamic Crystal, *J. Am. Chem. Soc.*, 2013, **135**, 5230–5233.
46 M. Mączka, A. Nowok, J. K. ZarÈ©ba, D. Stefańska, A. Gągor, M. Trzebiatowska and A. Sieradzki, Near-Infrared Phosphorescent Hybrid Organic–Inorganic Perovskite with High-Contrast Dielectric and Third-Order Nonlinear Optical Switching Functionalities, *ACS Appl. Mater. Interfaces*, 2022, **14**, 1460–1471.
47 M. Rok, A. Ciżman, B. Zarychta, J. K. Zaręba, M. Trzebiatowska, M. Mączka, A. Stroppa, S. Yuan, A. E. Phillips and G. Bator, Cyano-bridged perovskite $[(CH_3)_3NOH]_2[KM(CN)_6]$, [M: Fe(iii), and Co(iii)] for high-temperature multi-axial ferroelectric applications with enhanced thermal and nonlinear optical performance, *J. Mater. Chem. C*, 2020, **8**, 17491–17501.
48 C. Shi, C.-H. Yu and W. Zhang, Predicting and Screening Dielectric Transitions in a Series of Hybrid Organic–Inorganic Double Perovskites via an Extended Tolerance Factor Approach, *Angew. Chem., Int. Ed.*, 2016, **55**, 5798–5802.
49 A. E. Phillips and A. D. Fortes, Crossover between Tilt Families and Zero Area Thermal Expansion in Hybrid Prussian Blue Analogues, *Angew. Chem., Int. Ed.*, 2017, **56**, 15950–15953.
50 C. Shi, Z.-X. Gong, Q.-W. Wang, X.-B. Han and W. Zhang, Role of the B′-site metal ion in the framework structures

and dielectric transitions in host–guest type cyanometalates $(HIm)_2[B'Co(CN)_6]$ (HIm = imidazolium cation), *CrystEngComm*, 2020, **22**, 1848–1852.

51 W.-J. Xu, K.-P. Xie, Z.-F. Xiao, W.-X. Zhang and X.-M. Chen, Controlling Two-Step Phase Transitions and Dielectric Responses by A-Site Cations in Two Perovskite-like Coordination Polymers, *Cryst. Growth Des.*, 2016, **16**, 7212–7217.

52 M. Rok, B. Zarychta, M. Moskwa, B. Dziuk, W. Medycki and G. Bator, Structural phase transitions coupled with prominent dielectric anomalies and dielectric relaxation in $[(CH_3)_3NH]_2[KCo(CN)_6]$ and mixed $[(CH_3)_3NH]_2[KFe_xCo_{1-x}(CN)_6]$ double perovskite hybrids, *Dalton Trans.*, 2020, **49**, 1830–1838.

53 W.-J. Xu, S.-L. Chen, Z.-T. Hu, R.-B. Lin, Y.-J. Su, W.-X. Zhang and X.-M. Chen, The cation-dependent structural phase transition and dielectric response in a family of cyano-bridged perovskite-like coordination polymers, *Dalton Trans.*, 2016, **45**, 4224–4229.

54 M. Rok, J. K. Prytys, V. Kinzhybalo and G. Bator, Flexible crystals of perovskite-like coordination polymers with a tunable and switchable organic guest: $(CH_3NH_3)_2[KFe(CN)_6]$ and $(CH_3NH_3)_2[KCo(CN)_6]$, *Dalton Trans.*, 2017, **46**, 2322–2331.

55 M. Trzebiatowska, A. Gągor, L. Macalik, P. Peksa and A. Sieradzki, Phase transition in the extreme: a cubic-to-triclinic symmetry change in dielectrically switchable cyanide perovskites, *Dalton Trans.*, 2019, **48**, 15830–15840.

56 Z.-X. Gong, Q.-W. Wang, J.-J. Ma, J.-Y. Jiang, D.-Y. E, Z.-Q. Li, F.-W. Qi and H. Liang, Reversible structural phase transitions and switchable dielectric behaviours in a cyanometallate-based double perovskite-type cage compound: $[C_3H_4NS]_2[KCo(CN)_6]$, *Mater. Chem. Front.*, 2020, **4**, 918–923.

57 W. Zhang, Y. Cai, R.-G. Xiong, H. Yoshikawa and K. Awaga, Exceptional Dielectric Phase Transitions in a Perovskite-Type Cage Compound, *Angew. Chem., Int. Ed.*, 2010, **49**, 6608–6610.

58 G. Kieslich, S. Sun and A. K. Cheetham, Solid-state principles applied to organic–inorganic perovskites: new tricks for an old dog, *Chem. Sci.*, 2014, **5**, 4712–4715.

59 D. E. Zelmon, D. L. Small and D. Jundt, Infrared corrected Sellmeier coefficients for congruently grown lithium niobate and 5 mol. % magnesium oxide–doped lithium niobate, *J. Opt. Soc. Am. B*, 1997, **14**, 3319–3322.

60 H. T. Luo, T. Tkaczyk, E. L. Dereniak, K. Oka and R. Sampson, High birefringence of the yttrium vanadate crystal in the middle wavelength infrared, *Opt. Lett.*, 2006, **31**, 616–618.

61 G. Ghosh, Dispersion-equation coefficients for the refractive index and birefringence of calcite and quartz crystals, *Opt. Commun.*, 1999, **163**, 95–102.

62 J. R. DeVore, Refractive Indices of Rutile and Sphalerite, *J. Opt. Soc. Am.*, 1951, **41**, 416–419.

63 Z. Guoqing, X. Jun, C. Xingda, Z. Heyu, W. Siting, X. Ke, D. Peizhen and G. Fuxi, Growth and spectrum of a novel birefringent α-BaB_2O_4 crystal, *J. Cryst. Growth*, 1998, **191**, 517–519.

64 J. Wang, Y. Ma, Z. Wang, X. Liu, S. Han, Y. Liu, W. Guo, J. Luo and Z. J. M. Sun, Unusual ferroelectric-dependent birefringence in 2D trilayered perovskite-type ferroelectric exploited by dimensional tailoring, *Matter*, 2022, **5**, 194–205.

65 H.-H. Chen, X.-G. Chen, Z.-K. Xu, H. Peng, Y. Qin, H.-P. Lv, X.-J. Song, S.-Q. Hu, L.-Y. Ji, J.-S. Zhou, R.-G. Xiong and W.-Q. Liao, A 3D Hybrid Perovskite Ferroelastic with Triclinic-to-Cubic Phase Transition Boosts Temperature/Pressure Dual On/Off Switchable Birefringence, *Angew. Chem., Int. Ed.*, 2025, e202503681.

66 H.-P. Lv, S.-Q. Hu, Y.-J. Bai, J.-S. Zhou, L.-Y. Ji, Z.-X. Wang, Y. Ai, Y. Qin and X.-G. Chen, Giant mechanical tunability by a coordination bond strategy in a 3D hybrid cyanide double perovskite ferroelastic with reconstructive phase transition, *Chem. Sci.*, 2025, **16**, 9109–9116.

67 N. Archana, M. Vijayasri and S. Parthiban, Mongrel synthesis of tin(IV) based 3-aminopyridine with hydrogen halides: Structural, optical, thermal analysis, DFT, Hirshfeld surface analysis and antibacterial investigations, *J. Mol. Struct.*, 2025, **1321**, 140239.

68 L. Khedhiri, E. Jeanneau, F. Lefebvre, M. Rzaigui and C. B. Nasr, Synthesis and Characterization of a new Cyclohexaphosphate, $(C_9H_{14}N)_4(H_3O)_2(P_6O_{18})$, *J. Chem. Sci.*, 2016, **128**, 1037–1045.

69 S. Chen, D.-C. Han, L. Ye and W.-X. Zhang, Three-Step Ferroelastic Transitions from Hexagonal to Triclinic Phases in a Hybrid Perovskite: (1-Fluoromethyl-1-methylpyrrolidine)$[CdCl_3]$, *Inorg. Chem.*, 2024, **63**, 7966–7972.

70 M. A. Carpenter, E. K. H. Salje and A. Graeme-Barber, Spontaneous strain as a determinant of thermodynamic properties for phase transitions in minerals, *Eur. J. Mineral.*, 1998, **10**, 621–691.

71 L. He, L. Zhou, P.-P. Shi, Q. Ye and D.-W. Fu, One-Dimensional Cadmium Thiocyanate Perovskite Ferroelastics Tuned by Halogen Substitution, *Chem. Mater.*, 2019, **31**, 10236–10242.

72 Y.-J. Cao, L. Zhou, P.-P. Shi, Q. Ye and D.-W. Fu, H/F substituted perovskite compounds with above-room-temperature ferroelasticity: $[(CH_3)_4P][Cd(SCN)_3]$ and $[(CH_3)_3PCH_2F][Cd(SCN)_3]$, *Chem. Commun.*, 2019, **55**, 8418–8421.

73 H. Ye, X.-X. Chen, D.-X. Liu, B.-Q. Zhao, Y.-B. Li, Y. Zeng, W.-X. Zhang and X.-M. Chen, Subtly tuning intermolecular hydrogen bonds in hybrid crystals to achieve ultrahigh-temperature molecular ferroelastic, *Chem. Sci.*, 2022, **13**, 14124–14131.

74 W.-J. Xu, P. Zelenovskii, A. Tselev, L. Verissimo, K. Romanyuk, W. Yuan, W.-X. Zhang, A. Kholkin and J. Rocha, A hybrid double perovskite ferroelastic exhibiting the highest number of orientation states, *Chem. Commun.*, 2023, **59**, 11264–11267.

